

# HIGH-RESOLUTION HYBRID SIMULATIONS OF KINETIC PLASMA TURBULENCE AT PROTON SCALES

LUCA FRANCI<sup>1,2</sup>, SIMONE LANDI<sup>1,3</sup>, LORENZO MATTEINI<sup>4,1</sup>, ANDREA VERDINI<sup>1,5</sup>, PETR HELLINGER<sup>6</sup>

(Dated: June 22, 2015)  
*Draft version June 22, 2015*

## ABSTRACT

We investigate properties of plasma turbulence from magneto-hydrodynamic (MHD) to sub-ion scales by means of two-dimensional, high-resolution hybrid particle-in-cell simulations. We impose an initial ambient magnetic field, perpendicular to the simulation box, and we add a spectrum of large-scale magnetic and kinetic fluctuations, with energy equipartition and vanishing correlation. Once the turbulence is fully developed, we observe a MHD inertial range, where the spectra of the perpendicular magnetic field and the perpendicular proton bulk velocity fluctuations exhibit power-law scaling with spectral indices of  $-5/3$  and  $-3/2$ , respectively. This behavior is extended over a full decade in wavevectors and is very stable in time. A transition is observed around proton scales. At sub-ion scales, both spectra steepen, with the former still following a power law with a spectral index of  $\sim -3$ . A  $-2.8$  slope is observed in the density and parallel magnetic fluctuations, highlighting the presence of compressive effects at kinetic scales. The spectrum of the perpendicular electric fluctuations follows that of the proton bulk velocity at MHD scales, and flattens at small scales. All these features, which we carefully tested against variations of many parameters, are in good agreement with solar wind observations. The turbulent cascade leads to an overall proton energization with similar heating rates in the parallel and perpendicular directions. While the parallel proton heating is found to be independent on the resistivity, the number of particles per cell and the resolution employed, the perpendicular proton temperature strongly depends on these parameters.

*Subject headings:* plasmas – solar wind – turbulence

## 1. INTRODUCTION

Turbulence is an ubiquitous phenomenon in space and astrophysical plasmas. Although it is generally driven by violent events or instabilities at large scales, a further cascade is responsible for transferring energy via nonlinear coupling from the large injection scale to much smaller scales, through the ion and the electron characteristic regimes, where they are eventually dissipated. In-situ measurements in the solar wind represent a unique opportunity to study those processes, since they provide observations in a huge range of scales (see for example reviews by Tu & Marsch (1995); Matthaeus & Velli (2011); Alexandrova et al. (2013); Bruno & Carbone (2013)). The estimated turbulent energy cascade rate (e.g., MacBride et al. 2008; Cranmer et al. 2009; Hellinger et al. 2011, 2013) is comparable to the proton heating needed to explain the non adiabatic evolution of the solar wind plasma during its expansion (e.g., Marsch et al. 2004; Matteini et al. 2007). This suggests that turbulence plays an active role in transferring energy from electromagnetic fields to particles and heats the solar wind plasma. However, the processes that ultimately lead to heating in a collisionless turbulent medium are

still unknown.

Supporting evidence of a turbulent cascade is provided by the observed energy spectra, which exhibit a power-law behavior over a large range of scales, spanning nearly four decades in frequency. The spectral index of magnetic and kinetic spectra varies with the temperature of the solar wind streams (Grappin et al. 1990, 1991). The latter is in turn correlated with the stream speed and, although to a smaller extent, with the degree of Alfvénicity, i.e., the correlation between kinetic and magnetic fluctuations (Podesta & Borovsky 2010; Chen et al. 2013a). However, on average, at fluid-like scales a typical Kolmogorov power law with spectral index  $-5/3$  is usually observed for magnetic fluctuations, while kinetic energy spectra show a Iroshnikov-Kraichnan  $-3/2$  scaling (Podesta et al. 2006, 2007; Tassein et al. 2009; Salem et al. 2009; Chen et al. 2011b; Wicks et al. 2011). In particular, such scaling is found to be typical of regimes with balanced turbulence, i.e., zero cross-helicity (Podesta & Borovsky 2010). In the same range of scales, a certain amount of residual energy, i.e., an excess of magnetic to kinetic energy, is typically observed, following a well defined power-law scaling with an index of  $-2$  (Chen et al. 2013a). The electric field spectrum is observed to follow the velocity spectrum, when measured in the solar wind frame (Chen et al. 2011a), while density fluctuations exhibit a Kolmogorov-like cascade.

In the vicinity of the ion inertial length scale, a break in the magnetic field power spectrum is observed (Beinroth & Neubauer 1981; Goldstein et al. 1994; Leamon et al. 1998, 1999). Early observations of the spectrum of magnetic fluctuations in a restricted region above the break found a power-law scaling with a variable spectral index, ranging from  $-2$  to  $-4$  (e.g., Leamon et al. 1998,

<sup>1</sup> Dipartimento di Fisica e Astronomia, Università degli Studi di Firenze, Largo E. Fermi 2, I-50125 Firenze, Italy

<sup>2</sup> INFN - Sezione di Firenze, Via G. Sansone 1, I-50019 Sesto F.no (Firenze), Italy

<sup>3</sup> INAF - Osservatorio Astrofisico di Arcetri, Largo E. Fermi 5, I-50125 Firenze, Italy

<sup>4</sup> Space and Atmospheric Physics Group, Imperial College London, London SW7 2AZ, UK

<sup>5</sup> Solar-Terrestrial Center of Excellence, Royal Observatory of Belgium, Brussels, Belgium

<sup>6</sup> Astronomical Institute, AS CR, Boční II/1401, CZ-14100 Prague, Czech Republic

1999; Bale et al. 2005; Smith et al. 2006; Alexandrova et al. 2008b,a; Kiyani et al. 2009; Sahraoui et al. 2009; Chen et al. 2010; Salem et al. 2012). However, more recently, observations extended to smaller scales suggest a general convergence of the spectra towards a spectral index of  $-2.8$  (Kiyani et al. 2009; Alexandrova et al. 2009; Sahraoui et al. 2010), or towards a power-law scaling of  $-8/3$ , exponentially damped at sub-electron scales (Alexandrova et al. 2012). Magnetic fluctuations at sub proton scales are also characterized by a reduction of the magnetic variance anisotropy (Podesta & TenBarge 2012), and by an increase of the magnetic compressibility (Alexandrova et al. 2008a; Salem et al. 2012; Kiyani et al. 2013), suggesting a change in the nonlinear interactions ruling the cascade. This is partially confirmed by the measured increase of the intermittency at ion scales (Alexandrova et al. 2008a; Kiyani et al. 2009, 2013; Wu et al. 2013; Chen et al. 2014), although a clear behavior of the flatness at smaller, sub-ion, scales has not been identified yet.

There are observational indications that, below the ion inertial length scale, the electric field spectrum decouples from the velocity field and flattens (Bale et al. 2005; Salem et al. 2012) but, due to the high noise level, present data do not allow to determine the existence of a power-law scaling at sub-ion scales. Density fluctuations show a plateau just before the ion scales, while they follow a power law between the ion and the electron scales, with the same spectral index as the one of the magnetic field spectrum (Chen et al. 2012, 2013b).

Properties of turbulence have been extensively analyzed by means of direct numerical simulations (DNS), employing many different methods and models. Although several features of the solar wind turbulence can be partially recovered, we are still far from a comprehensive picture. At large fluid-like scales, DNS of incompressible MHD and reduced MHD (RMHD) return a spectral index for the total energy close to  $-2$ ,  $-5/3$ , or  $-3/2$  (e.g., Maron & Goldreich 2001; Müller et al. 2003; Müller & Grappin 2005; Mason et al. 2008; Perez & Boldyrev 2009; Beresnyak & Lazarian 2009; Grappin & Müller 2010; Boldyrev et al. 2011; Lee et al. 2010; Chen et al. 2011b; Beresnyak 2011; Perez et al. 2012). These spectral indices are associated to the different nature of the nonlinear interactions regulating the cascade and the cascade rate. Moreover, within the inertial range, a transition between different regimes can occur (Mininni & Pouquet 2007; Verdini & Grappin 2012). More sophisticated DNS, including other physical processes like expansion effects (Dong et al. 2014), Hall-MHD (e.g., Matthaeus et al. 2003; Gómez et al. 2008; Shaikh & Shukla 2009; Shaikh & Zank 2009), reduced Hall MHD (Gómez et al. 2013), gyrokinetic (Howes et al. 2008; TenBarge et al. 2013), and hybrid particle-in-cell (PIC) simulations (Vasquez & Markovskii 2012), all produce spectral indices consistent with  $-5/3$ . Anyway, the restricted width of the inertial range prevents firm conclusions.

As far as the small kinetic scales are concerned, DNS including proton and electron physics return a qualitatively unified picture. At sub-proton scales, they reproduce an increase of the ratio of the electric to magnetic power, together with a flattening of the electric field spectrum (e.g., Dmitruk & Matthaeus 2006; Howes et al. 2008, 2011; Servidio et al. 2012; Gómez et al. 2013;

Perrone et al. 2013; Parashar et al. 2014; Passot et al. 2014; Valentini et al. 2014; Servidio et al. 2015), and a transition to a steeper spectrum for the magnetic field power near the ion scales (e.g., Matthaeus et al. 2003; Dmitruk & Matthaeus 2006; Parashar et al. 2010; Servidio et al. 2012; Vasquez & Markovskii 2012; Rodriguez Imazio et al. 2013; Valentini et al. 2014). However, a unique spectral index cannot be identified for the magnetic field spectrum at proton scales. Early works in Hall MHD (Shaikh & Shukla 2009; Martin et al. 2013), Electron-MHD (Biskamp et al. 1999; Ng et al. 2003; Cho & Lazarian 2004, 2009; Shaikh 2009), and gyrokinetic (Howes et al. 2008) reported a spectral index of  $-7/3$  for the magnetic field at sub-ion scales. More recently, steeper spectra have also been observed: a spectral index of  $-2.8$  in gyrokinetic (Howes et al. 2011; TenBarge & Howes 2013; TenBarge et al. 2013) and finite Larmor radius (FLR)-Landau fluid simulations (Passot et al. 2014), or a  $-8/3$  power law both in 3D electron-MHD (Meyrand & Galtier 2013) and in strong kinetic-Alfvén turbulence (Boldyrev & Perez 2012). Magnetic spectral indices in-between about  $-2.6$  and  $-3$  have also been observed in full PIC simulations (e.g., Camporeale & Burgess 2011; Chang et al. 2011; Wan et al. 2012; Karimabadi et al. 2013; Wu et al. 2013).

In situ measurements of the proton velocity distribution functions show the presence of an ubiquitous temperature anisotropy between the direction parallel and perpendicular to the mean magnetic field (Marsch et al. 1982; Hellinger et al. 2006), and a non adiabatic evolution of the solar wind plasma during its expansion (Marsch et al. 2004; Matteini et al. 2007), thus suggesting, as already mentioned, an active role played by the turbulence in exchanging energy between fields and particles. Hybrid PIC simulations have shown an overall (macroscopic) collisionless proton heating, with signatures of a preferential proton heating in the perpendicular direction with respect to the ambient mean magnetic field (e. g. Parashar et al. 2009; Markovskii et al. 2010; Markovskii & Vasquez 2011; Vasquez & Markovskii 2012; Verscharen et al. 2012; Parashar et al. 2014). Vlasov-Hybrid simulations suggest that non-Maxwellian kinetic effects, such as temperature anisotropies, can be produced by the turbulence, mostly concentrated in regions near and around the peaks of the current density (Servidio et al. 2012; Valentini et al. 2014; Perrone et al. 2014; Servidio et al. 2015).

In our previous work (Franci et al. 2015) (named hereafter as Letter 1), we presented results from a high-resolution hybrid (fluid electrons, PIC protons) two-dimensional (2D) simulations of turbulence. The spectra of various fluctuations (magnetic, kinetic, density and electric field), along with the magnetic compressibility and the non-dimensional ratio of the density and the magnetic fluctuations, simultaneously matched several features observed in the solar wind. In particular, for the magnetic field we showed that high-resolution hybrid simulations, although limited to a 2D geometry, are able to capture the nonlinear dynamics at fluid-like MHD scales and at subproton scales, both within the same numerical domain. In this paper, we analyze in further detail the spectral properties of several fields, also showing their stability with time. Moreover, we investigate the shape of the electric field spectrum, by estimating

the separated contributions from different terms in the generalized Ohm's law. Finally, we study the proton temperature anisotropy and the proton heating, also quantifying the dependence from the resistivity coefficient and the number of particles-per-cell (ppc) employed in the simulations.

The paper is organized as follows: In Section 2, we describe the numerical setup employed, define the physical units and normalizations in the code, and provide the parameters of our initial conditions. In Section 3, we describe the results of the performed simulations. In Section 4, we validate such results, by investigating the importance of a careful choice of some relevant numerical parameters. Finally, in Section 5, we summarize the achievements of our simulations and discuss them in the framework of both observational and previous numerical and theoretical studies.

## 2. NUMERICAL SETUP AND INITIAL CONDITIONS

We make use of a 2D hybrid code, where electrons are considered as a massless, charge neutralizing fluid with a constant temperature, whereas ions are described by a PIC model and are advanced by the Boris' scheme, which requires the fields to be known at a half time step ahead of the particle velocities. This is achieved by advancing the current density to this time step with only one computational pass through the particle data at each time step (Matthews 1994).

The characteristic spatial and temporal units used in this model are the proton inertial length  $d_p = c/\omega_p$ ,  $\omega_p = (4\pi ne^2/m_p)^{1/2}$  being the proton plasma frequency, and the inverse proton gyrofrequency  $\Omega_p^{-1} = (eB_0/m_pc)^{-1}$ , respectively. Magnetic fields are expressed in units of the magnitude of the ambient magnetic field, i.e.,  $B_0$ , while velocities are expressed in units of the Alfvén velocity, i.e.,  $v_A = B_0/(4\pi nm_p)^{1/2}$ . The plasma beta for a given plasma species, protons ( $p$ ) or electrons ( $e$ ), is  $\beta_{p,e} = 8\pi n K_B T_{p,e}/B_0^2$ . Quantities and symbols used in these definitions are: the speed of light,  $c$ , the number density,  $n$ , which is assumed to be equal for proton and electrons ( $n_p = n_e = n$ ), the magnitude of the electronic charge,  $e$ , the proton mass,  $m_p$ , the Boltzmann's constant,  $K_B$ , and the proton and electron temperatures,  $T_{p,e}$ .

The 2D computational domain lies in the  $(x, y)$  plane, while the ambient magnetic field  $\mathbf{B}_0$  is along the  $z$ -direction. Accordingly, each field  $\Psi$  will be decomposed in its perpendicular (in-plane) component,  $\Psi_\perp$ , and its parallel (out-of-plane, along  $\mathbf{z}$ ) component,  $\Psi_\parallel$ , with respect to  $\mathbf{B}_0$ . The only exceptions will be the proton beta and temperature, for which  $\perp$  and  $\parallel$  will denote directions with respect to the local magnetic field.

The adopted simulation box is a  $2048^2$  square grid. We tested different resolutions ( $\Delta x = \Delta y = 0.5, 0.25$  and  $0.125 d_p$ ), and consequently different box sizes ( $L_{\text{box}} = 1024, 512$  and  $256 d_p$ ), as well as different numbers of ppc, ranging from 500 to 8000 (see Table 1). The time step for the particle advance is  $\Delta t = 0.025 \Omega_p^{-1}$ , whereas the magnetic field  $\mathbf{B}$  is advanced with a smaller time step,  $\Delta t_B = \Delta t/10$ .

Initially, we assume a uniform number density  $n = 1$ , a proton parallel beta  $\beta_{p\parallel} = 0.5$ , and a temperature anisotropy  $A_p = T_{p\perp}/T_{p\parallel} = 1$ . Electrons are isotropic,

Run	$\Delta x$ ( $d_p$ )	$L_{\text{box}}$ ( $d_p$ )	$\eta$ ( $4\pi/\omega_p$ )	ppc
A	0.125	256	$5 \times 10^{-4}$	8000
B	0.125	256	$5 \times 10^{-4}$	4000
C	0.125	256	$5 \times 10^{-4}$	2000
D	0.125	256	$5 \times 10^{-4}$	1000
E	0.125	256	$5 \times 10^{-4}$	500
F	0.125	256	$1 \times 10^{-4}$	8000
G	0.125	256	$1 \times 10^{-3}$	8000
H	0.250	512	$1 \times 10^{-3}$	8000
I	0.500	1024	$2 \times 10^{-3}$	8000

TABLE 1  
LIST OF SIMULATIONS AND THEIR RELEVANT PARAMETERS

with  $\beta_e = 0.5$ . We add an initial spectrum of magnetic and velocity fluctuations in the  $(x, y)$  plane, composed of modes with  $-0.2 < k_{x,y} < 0.2$  in each direction and random phases. These initial fluctuations are characterized by energy equipartition and vanishing correlation between kinetic and magnetic fluctuations, and their global amplitude is  $B^{rms} \sim 0.24$ . Hereafter,

$$\Psi^{rms} = (\langle \Psi^2 \rangle - \langle \Psi \rangle^2)^{1/2} \quad (1)$$

will denote the root mean square value (rms) of a quantity  $\Psi$ , with  $\langle \Psi \rangle$  being its space-averaged value over the whole 2D simulation domain. The initial magnetic fluctuations can be expressed in the form

$$\mathbf{B}_\perp(x, y) = \frac{1}{2} \sum_{k_x, k_y} [\mathbf{B}_\perp(k_x, k_y) \times \exp(i(k_x x + k_y y + \phi(k_x, k_y))) + \text{c.c.}] \quad (2)$$

The initial bulk velocity fluctuations  $\mathbf{u}_\perp(t = 0)$  are assumed to have the same form as in Eq. (2), with different random phases.

We introduce two dimensionless quantities, i.e., the normalized cross helicity,  $\sigma_C$ , and the normalized residual energy,  $\sigma_R$ :

$$\sigma_C(x, y) = \frac{2 \mathbf{u} \cdot \mathbf{B}}{|\mathbf{u}|^2 + |\mathbf{B}|^2}, \quad (3)$$

$$\sigma_R(x, y) = \frac{|\mathbf{u}|^2 - |\mathbf{B}|^2}{|\mathbf{u}|^2 + |\mathbf{B}|^2}, \quad (4)$$

which define the two-dimensional geometry of the fluctuations. With the initial conditions we chose for the initial magnetic and bulk velocity fluctuations,  $\sigma_C$  and  $\sigma_R$  are both statistically very close to zero, even though they are not actually zero anywhere in the  $(x, y)$  plane.

A non-zero resistivity has been introduced in order to guarantee a satisfactory conservation of the total energy, with no claim to model any realistic physical process. Its value has been empirically fine-tuned by running different simulations (see Table 1). Further details about this point will be provided in Sec. 4.

## 3. RESULTS

We performed nine different simulations. Their main parameters are listed in Table 1. A label is assigned to each run in the first column, while in the other columns we report, from left to right: the spatial resolution,  $\Delta x$  ( $= \Delta y$ ), the length of the simulation box,  $L_{\text{box}}$ , the value of the resistivity coefficient,  $\eta$ , and the number of ppc.

Run A employs the best spatial resolution,  $\Delta x = \Delta y = 0.125 d_p$ , and the highest number of particles, i.e., 8000 ppc, corresponding to more than  $3 \times 10^{10}$  particles in the whole simulation domain. The resistive coefficient has been fine-tuned and set to the value  $\eta = 5 \times 10^{-4}$ , in units of  $4\pi\omega_p^{-1}$ . In Subsection 3.1 and 3.2 we will provide a detailed and quantitative analysis of the data produced by this run. The remaining simulations were performed in order to validate these results and to investigate the effects of the number of ppc (Runs B-E, see Table 1), the resistivity (Runs F-G), and the spatial resolution (Runs H-I). Their results will be discussed later, in Section 4.

### 3.1. Temporal and spatial evolution

In Fig. 1, the time evolution of a few quantities is shown up to  $500 \Omega_p^{-1}$ . The initial non-linear time associated to the maximum injection scale, i.e.,  $k^{\text{inj}} \sim 0.2 d_p^{-1}$ , can be estimated as  $t_{\text{NL}} \sim [k^{\text{inj}} \delta u_{k^{\text{inj}}}]^{-1} \sim 20 \Omega_p^{-1}$ , and corresponds to the minor ticks of the  $x$  axis. The total length of the simulation is approximately  $25 t_{\text{NL}}$ .

In the first panel, from top to bottom, we report the rms out-of-plane current density,  $\mathbf{J}_{\parallel}$ , and the rms out-of-plane vorticity,  $\omega_{\parallel}$ . The current increases quite rapidly, attains its maximum value just before  $t \sim 200 \Omega_p^{-1}$  and then slowly decreases. Since it represents a good indicator of the level of turbulent activity (Mininni & Pouquet 2009), we choose to perform a detailed analysis at  $t \sim 200 \Omega_p^{-1}$ , when the turbulence is expected to be fully developed. A vertical black dotted line marks this time in all four panels. The vorticity also increases quite rapidly, reaching an earlier and lower maximum value, and then it decreases extremely slowly.

The second panel of Fig. 1 shows the rms perpendicular  $\mathbf{B}_{\perp}$  and parallel  $\mathbf{B}_{\parallel}$  magnetic fluctuations (red lines), and the rms perpendicular  $\mathbf{u}_{\perp}$  and parallel  $\mathbf{u}_{\parallel}$  velocity fluctuations (blue lines). Perpendicular and parallel components are drawn with solid and dashed lines respectively.  $\mathbf{B}_{\perp}$  exhibits a small increase until  $t \sim 40 \Omega_p^{-1}$ , and then it decreases quite smoothly. On the other hand,  $\mathbf{u}_{\perp}$  decreases with a similar trend, but without showing any initial growth. This indicates that the turbulence is fed by the perpendicular components of both the magnetic and the velocity fluctuations, whose energy decreases slowly and sustains the cascade for the whole evolution. Contextually, the parallel components of both the magnetic and the velocity fluctuations rapidly originate from compressive effects, remaining much smaller than their perpendicular counterparts throughout the simulation.

In the third panel of Fig. 1, we report the space-averaged parallel and perpendicular proton temperatures, normalized to the initial value  $T_0$ ,  $\langle T_{p\parallel}/T_0 \rangle$  and  $\langle T_{p\perp}/T_0 \rangle$  respectively, together with the space-averaged proton temperature anisotropy,  $\langle A_p \rangle = \langle T_{p\perp}/T_{p\parallel} \rangle$ . We recall here that  $T_{\parallel}$  and  $T_{\perp}$  are defined with respect to the local magnetic field. Since  $\langle A_p \rangle = 1$  is imposed at  $t = 0$ ,  $T_{p\parallel}$  and  $T_{p\perp}$  share the same initial value,  $T_0$ . In the very first part of the evolution, the former shows a little and sudden decrease, after which both increase with almost the same rate. The parallel and perpendicular energy gains, at the end of the simulation, i.e., at  $t = 500 \Omega_p^{-1}$ , are approximately 6% and 8% respectively.

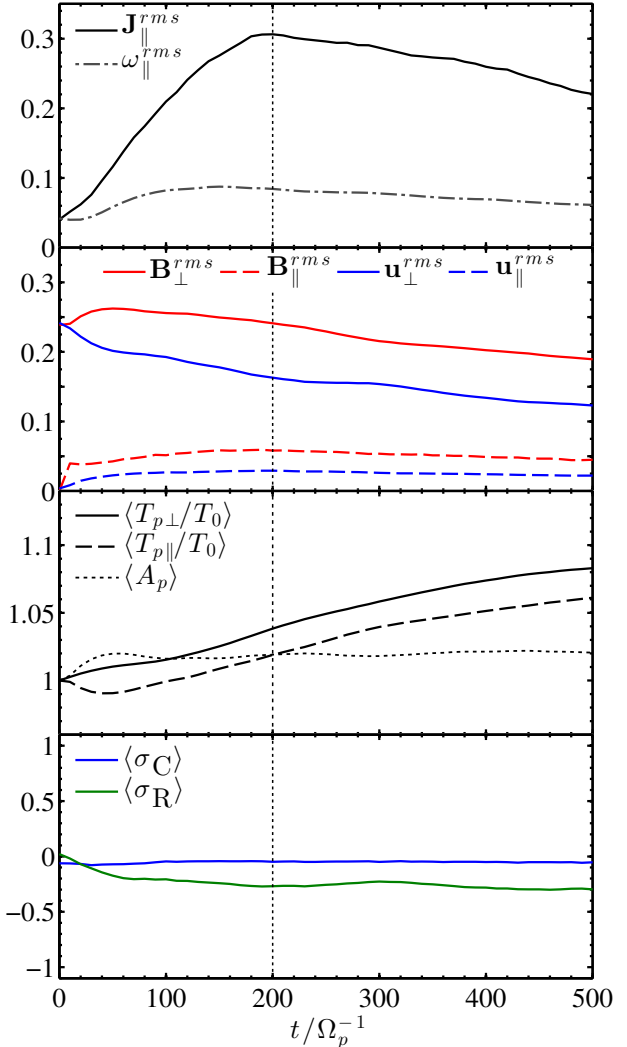


FIG. 1.— Time evolution of space-averaged quantities. From top to bottom: the rms out-of-plane current density,  $\mathbf{J}_{\parallel}$ , and the rms out-of-plane vorticity,  $\omega_{\parallel}$  (*first panel*); the rms perpendicular  $\mathbf{B}_{\perp}$  and parallel  $\mathbf{B}_{\parallel}$  magnetic fluctuations, and the rms perpendicular  $\mathbf{u}_{\perp}$  and parallel  $\mathbf{u}_{\parallel}$  velocity fluctuations (*second panel*); the mean values of the normalized perpendicular and parallel proton temperatures,  $T_{p\perp}/T_0$  and  $T_{p\parallel}/T_0$ , and of the proton temperature anisotropy,  $A_p$  (*third panel*); the mean values of the normalized cross helicity,  $\sigma_C$ , and of the normalized residual energy,  $\sigma_R$  (*fourth panel*). In all panels, a vertical black dotted line marks the time of the maximum turbulent activity, i.e.,  $t = 200 \Omega_p^{-1}$ .

This small excess of perpendicular energy quickly arises within  $\sim 2 t_{\text{NL}}$ , and it is preserved throughout the simulation, with the temperature anisotropy reaching a value  $\langle A_p \rangle \sim 1.02$  in correspondence of the maximum turbulent activity, and then remaining quite constant until the end of the simulation. A detailed discussion about the proton heating will be further provided in Subsection 4.2.

Lastly, in the bottom panel of Fig. 1, we show the space-averaged values of the normalized cross helicity,  $\sigma_C$ , and of the residual energy,  $\sigma_R$ , (see Eq. (3) and (4)). The former is very close to zero at the beginning of the simulation (as a result of the initially imposed random phases spectra), and it tends to maintain this value until the end. The latter, instead, decreases from zero to about  $-0.3$  in very few non-linear times  $t_{\text{NL}}$ , showing a

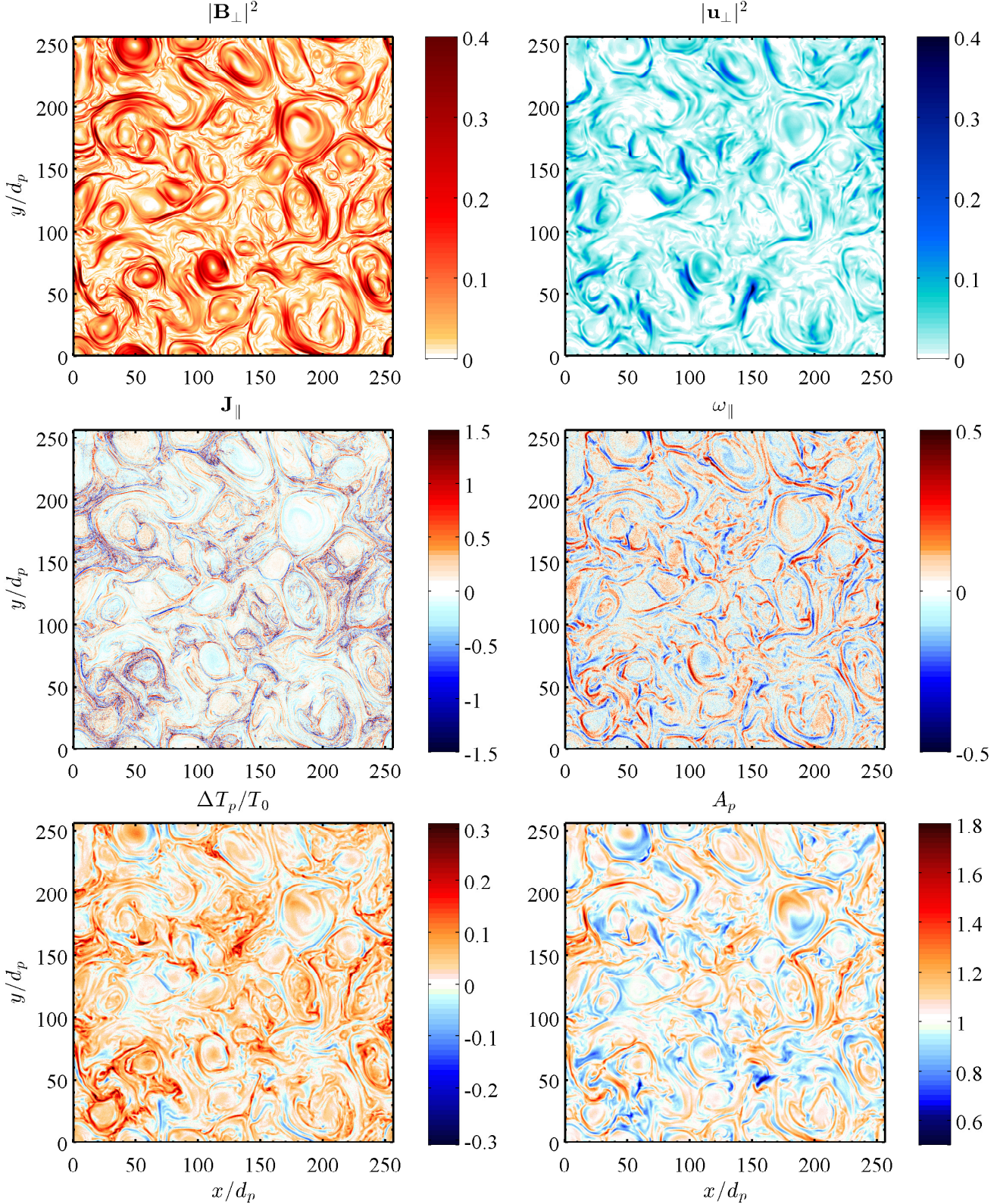


FIG. 2.— Contour plots of six different quantities on the  $(x, y)$  plane at  $t = 200 \Omega_p^{-1}$ : the amplitude of the perpendicular magnetic fluctuations,  $\mathbf{B}_\perp^2$  (upper-left panel), and of the perpendicular velocity fluctuations,  $\mathbf{u}_\perp^2$  (upper-right panel), the out-of-plane current density,  $\mathbf{J}_\parallel$  (middle-left panel), and vorticity,  $\omega_\parallel$  (middle-right panel), the proton temperature variation normalized to the initial temperature,  $\Delta T_p/T_0$  (bottom-left panel), and the proton temperature anisotropy,  $A_p$  (bottom-right panel).

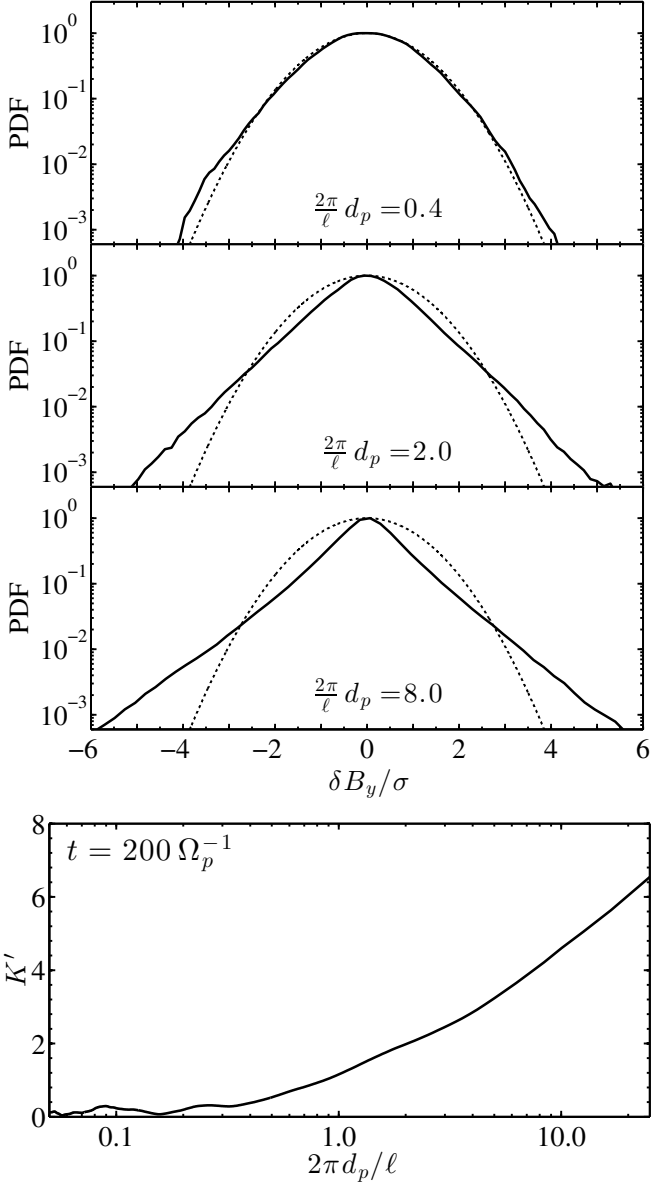


FIG. 3.— Top panel: PDFs of the increments of the perpendicular magnetic field component  $B_y$  along  $x$  at  $t = 200 \Omega_p^{-1}$ , corresponding to  $2\pi d_p/\ell = 0.4$ ,  $2\pi d_p/\ell = 2$  and  $2\pi d_p/\ell = 8$  (from top to bottom). In each panel, a Gaussian function with the same variance is plotted with a dashed line as a reference. Bottom panel: Excess kurtosis of the same quantity, computed at the same time.

global excess of the magnetic energy over the kinetic energy. These asymptotic values are reached very quickly, as a consequence of the relaxation from the initial random relative orientation of the velocity and the magnetic fluctuations towards a strongly aligned state. Despite the steady time evolution of their space-averaged values, both  $\sigma_C$  and  $\sigma_R$  appear very patchy when looking at the spatial distribution throughout the 2D computational domain (not shown), exhibiting quite a wide excursion from -1 to 1 between different albeit close regions.

Summarizing the time evolution of all the above-mentioned quantities, we can divide the evolution of the system in three different stages:

1. a rapid re-adjustment and relaxation of the initial conditions, occurring within  $t \lesssim 40 \Omega_p^{-1} \sim 2 t_{NL}$

2. the onset of a turbulent cascade, fed by the perpendicular magnetic and velocity fluctuations, involving larger and larger scales on times of the order of  $t \sim 200 \Omega_p^{-1} \sim 10 t_{NL}$

3. a deacaying phase with slow and smooth variations of all rms quantities, during which the turbulence is fully developed and further sustained until at least  $t \sim 500 \Omega_p^{-1}$ , corresponding to  $\sim 25 t_{NL}$ .

Fig. 2 shows isocontours of six different quantities in the whole simulation domain, all computed at  $t = 200 \Omega_p^{-1}$ . In the upper-left panel, we report the magnitude of the perpendicular magnetic fluctuations,  $|\mathbf{B}_\perp|^2$ , showing the presence of coherent structures in the magnetic field, i.e., vortices and magnetic islands, embedded in a much more chaotic environment where stretched and twisted shapes emerge. In the upper-right panel, the magnitude of the perpendicular velocity fluctuations,  $|\mathbf{u}_\perp|^2$ , is shown to exhibit qualitatively the same kind of structures, but with lower intensity and much lower gradients. In some regions, high values of  $|\mathbf{u}_\perp|^2$  correspond to high values of  $|\mathbf{B}_\perp|^2$ , while in other regions the opposite situation holds. In the middle-left panel, we show the out-of-plane current density,  $J_\parallel = (\nabla \times \mathbf{B})_\parallel$ . Many thin current sheets form, since the very first phase of the evolution, mostly around and in-between vortices. Once formed, each current sheet is quickly disrupted into smaller and smaller pieces, contributing to the generation of smaller-scale structures. At the time of maximum turbulent activity, this results in the articulated pattern shown here. In the middle-right panel, the out-of-plane vorticity,  $\omega_\parallel = (\nabla \times \mathbf{u})_\parallel$ , is shown. It exhibits a structure similar to  $J_\parallel$ , with many thin layers, whose shape is however much more defined and clean in respect to  $J_\parallel$ . Peaks of  $\omega_\parallel$  and peaks of  $J_\parallel$  occupy approximately the same regions. In the bottom left panel, we report the proton temperature variation in respect to the initial proton temperature,  $\Delta T_p/T_0 = (T_p - T_0)/T_0$ , where  $T_p = (2T_{p\perp} + T_{p\parallel})/3$  is the average proton temperature measured at  $t = 200 \Omega_p^{-1}$ . Regions where  $\Delta T_p$  is locally both negative or positive are clearly present, and a resulting global proton temperature enhancement can be observed, as already inferred from Fig. 1. Interestingly, areas where a proton temperature enhancement occurs are located in the vicinity of current sheets (cf., (Servidio et al. 2012)). A more detailed analysis shows that strong currents exhibit a complex evolution, which involves splitting/dissociation and leads to a relevant proton energization.

In the bottom right panel, the proton temperature anisotropy,  $A_p$ , is shown. We observe a wide excursion between very close areas, the perpendicular proton temperature  $T_{p\perp}$  ranging from about half and almost twice the parallel one. Therefore, there is a strong local reshaping of particle distributions, leading to both perpendicular and parallel anisotropies (Servidio et al. 2014). Nevertheless, as inferable from Fig. 1, the relative difference between  $\langle T_{p\perp} \rangle$  and  $\langle T_{p\parallel} \rangle$  is about 2% at  $t = 200 \Omega_p^{-1}$ , meaning that globally no preferential enhancement along the perpendicular or parallel direction is achieved.

The small-scale coherent structures which have emerged by the time of maximum turbulent activity,

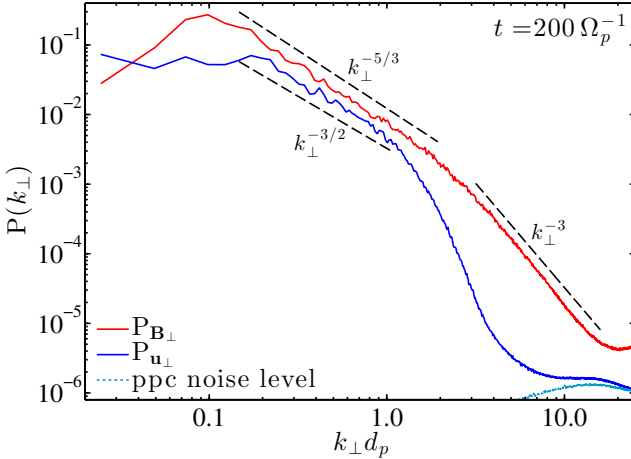


FIG. 4.— Power spectra of the perpendicular magnetic and velocity fluctuations,  $\mathbf{B}_\perp$  (red solid line) and  $\mathbf{u}_\perp$  (blue solid line), respectively. Power laws with different spectral indices are additionally shown in black dashed lines as a reference.

already observed in Fig. 2, can be related to the phenomenon of intermittency, since they are able to induce departures from self-similarity and enhanced dissipation. In order to look for intermittency in our data, we examine the non-Gaussian behavior of the probability density function (PDF) of a MHD primitive variable. In particular, we compute the PDFs at  $t = 200 \Omega_p^{-1}$  by taking increments of one of the perpendicular magnetic field components, i.e.,  $\mathbf{B}_y$ , along the other perpendicular direction, i.e.,  $x$ , for three different spatial separations,  $\ell$ . In the three top panels of Fig. 3, we show three PDFs, computed for  $2\pi d_p/\ell = 0.4$ , which is approximatively in the middle of the inertial range (upper panel),  $2\pi d_p/\ell = 2$ , which is the scale corresponding to the ion spectral break (middle panel) and  $2\pi d_p/\ell = 8$ , which is well inside the kinetic range (bottom panel). A Gaussian function with the same variance is plotted with a dashed line in each panel as a reference. The distribution of magnetic fluctuations is clearly different at different scales: it is closer to a normal distribution at very large scales, it shows a significant deviation at intermediate scales, and it displays very extended tails at small scales. In order to quantify the level of intermittency, we compute the fourth central moment  $K$  (or kurtosis) of the distributions. In the bottom panel of Fig. 3, we show the excess kurtosis  $K' = K - 3$ , computed from the increments of  $\mathbf{B}_y$  along  $x$ , as a function of  $2\pi d_p/\ell$ , again at  $t = 200 \Omega_p^{-1}$ . This quantity is clearly very close to zero up to the injection scale, i.e.,  $k_\perp d_p \lesssim 0.2$ , and the it steadily increases through the inertial range and down to sub-proton scales.

### 3.2. Spectral properties

Since the small-scale structures shown in Fig. 2 exhibit random orientations, and therefore the two-dimensional spectra of all fluctuations can be assumed statistically isotropic, we can perform a quantitative analysis of the turbulent cascade by computing the omnidirectional spectra. These are defined as

$$P_\Psi(k_\perp) \equiv \delta\Psi^2(k_\perp)/k_\perp = \sum_{|\mathbf{k}_\perp|=k_\perp} \hat{\Psi}_{2D}^2(\mathbf{k}_\perp), \quad (5)$$

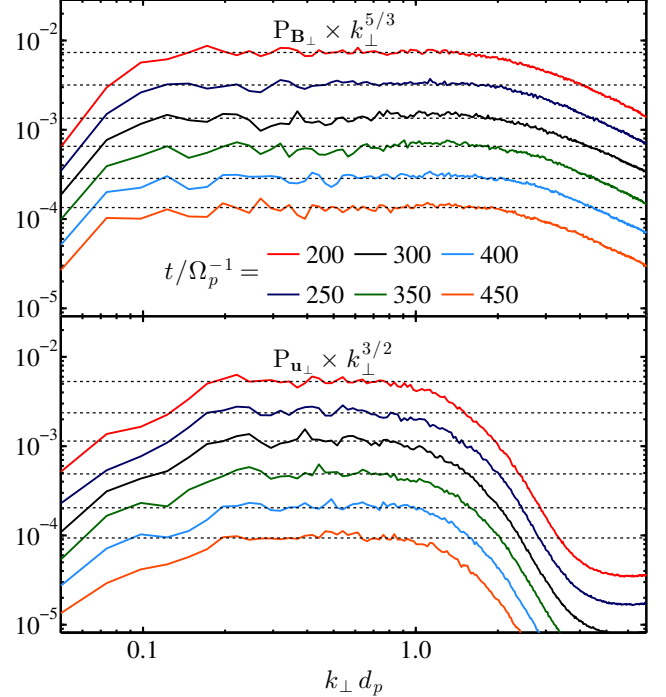


FIG. 5.— Top panel: Power spectra of the perpendicular magnetic fluctuations,  $\mathbf{B}_\perp$ , compensated by  $k_\perp^{5/3}$ . Each of them is the time average in the interval  $[\tilde{t} - 20\Omega_p^{-1}, \tilde{t} + 20\Omega_p^{-1}]$ , where  $\tilde{t}$  is the time reported in the legend. Note that all of them have been suitably rescaled for the sake of clarity, so that they did not overlapped each other. Horizontal dotted black lines are additionally shown. Bottom panel: The same as in the upper panel but for the perpendicular velocity fluctuations,  $\mathbf{u}_\perp$ , compensated by  $k_\perp^{3/2}$ .

where  $\hat{\Psi}$  are the Fourier coefficients of a given quantity  $\Psi$ , and  $\delta\Psi(k_\perp)$  is the amplitude of the fluctuation  $\Psi$  at the scale  $k_\perp$ .

In Fig. 4, we show the spectra of the perpendicular magnetic and velocity fluctuations, drawn with red and blue solid lines respectively, at  $t = 200 \Omega_p^{-1}$ . We clearly observe two power-law ranges, separated by a smooth spectral break at a scale of the order of the proton inertial length,  $k_\perp d_p \sim 2$ . In Letter 1, we showed the spectra of the total magnetic and velocity fluctuations, which exhibit a very similar behavior, since the perpendicular components are the dominant ones for both field.

In particular, in the inertial range the spectrum of the perpendicular magnetic fluctuations follows a Kolmogorov  $k_\perp^{-5/3}$  power-law scaling over a full decade in wavenumber, approximately between  $k_\perp d_p = 0.1$  and 2. Simultaneously, the perpendicular proton bulk velocity fluctuations exhibit a less steep slope, with an Iroshnikov-Kraichnan scaling of  $k_\perp^{-3/2}$ , over a little less than a decade, in the range  $0.2 \lesssim k_\perp d_p \lesssim 1$ . Moreover, an excess of magnetic energy over kinetic energy is observed, coherently with the negative value of the normalized residual energy  $\sigma_R$  already shown in the bottom panel of Fig. 1.

At kinetic scales, the spectra of both fields steepen, due to the presence of both kinetic and dissipative (resistive) effects. The spectrum of  $\mathbf{u}_\perp$  quickly drops with an exponential trend above  $k_\perp d_p \sim 1$ , until it clearly saturates to the noise level due to the finite number of ppc,

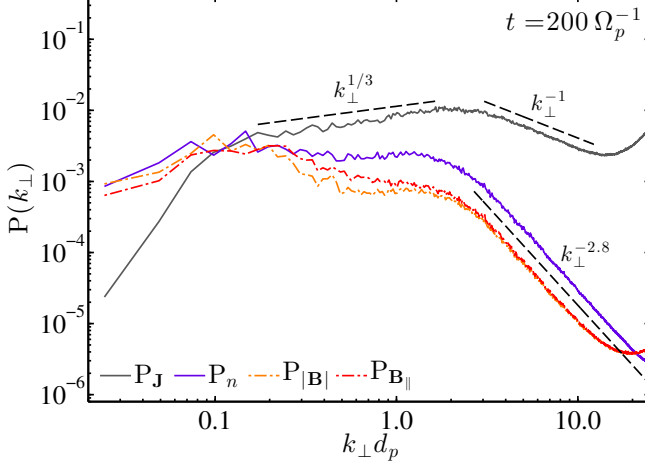


FIG. 6.— Spectra of the total current density,  $\mathbf{J}$  (grey line), of the density fluctuations,  $n$  (purple line), of the magnitude of the magnetic field,  $|\mathbf{B}|$  (orange line), and of its parallel component,  $\mathbf{B}_{\parallel}$  (red dot-dashed line). Power laws with different spectral indices are additionally drawn in black dashed lines, as a reference.

corresponding to the spectrum at  $t = 0$ . The spectrum of the magnetic fluctuations, on the contrary, continue to follow a power-law scaling also at sub-proton scales, although with a steeper spectral index, of the order of  $-3$ . For  $k_{\perp}d_p \gtrsim 10$ ,  $P_{\mathbf{B}_{\perp}}$  does not show an exponential damping, as one would expect for resistive dissipation, but a small increase instead, since the adopted resistive coefficient is slightly smaller than the optimal value.

As discussed, the maximum level of turbulent activity occurs at  $t \sim 200 \Omega_p^{-1}$ , which is about ten times the initial nominal nonlinear time  $t_{NL}$ . This can be explained with the fact that at  $t = 0$  we inject energy through several modes within the range  $[k_0, k^{inj}]$ , where  $k_0$  is the largest scale corresponding to the computational box size, i.e.,  $k_0 = 2\pi/(256 d_p) \sim 0.025 d_p^{-1}$ . The nominal nonlinear time  $t_{NL}|_{t=0}$  is different for each mode, being longer for lower  $k$ -vectors. As the system evolves, the injection scale gets larger and larger and most of the initial modes are involved in the development of the turbulent cascade at  $t = 200 \Omega_p^{-1}$ . Since modes with lower  $ks$  keep feeding energy at large scales even afterwards, we expect turbulence to be still sustained also at later times.

In Fig. 5 we show the spectra of the perpendicular magnetic fluctuations, compensated by  $k_{\perp}^{5/3}$  (top panel), and the spectra of the perpendicular velocity fluctuations, compensated by  $k_{\perp}^{3/2}$  (bottom panel), computed at regular intervals of  $50 \Omega_p^{-1}$ , from the maximum of turbulent activity to almost the end of the simulation. Here, the spectrum at a given time  $\tilde{t}$  is the time-average between five different spectra corresponding to  $\tilde{t}, \tilde{t} \pm 10 \Omega_p^{-1}$  and  $\tilde{t} \pm 20 \Omega_p^{-1}$ . The power-law scaling for both the magnetic and the velocity fluctuations are very well maintained, over about the same range, at all times  $t > 200 \Omega_p^{-1}$ , indicating that the turbulence decays in a self-similar way. Note that spectra corresponding to different times have been slightly shifted along the vertical axis, in order to avoid overlapping.

In Fig. 6, we show the spectra of the magnitude of the magnetic field,  $|\mathbf{B}|$  (orange), of its parallel compo-

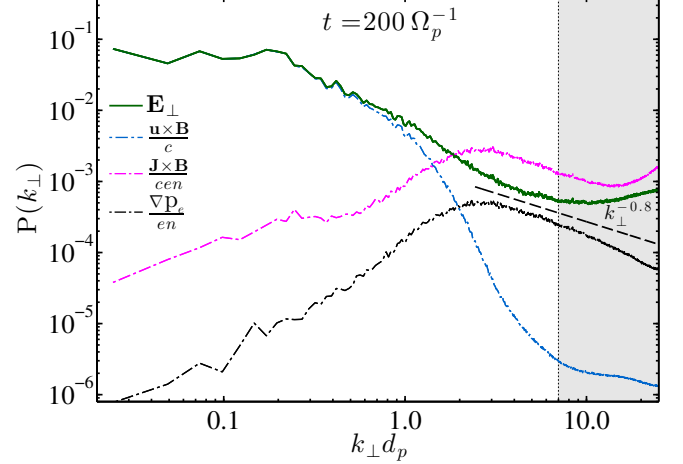


FIG. 7.— Spectrum of the perpendicular electric field,  $E_{\perp}$  (green solid line) and energy associated to the different terms of Eq. (6) (the term containing the resistive coefficient is negligible). A power law with a spectral index of  $-0.8$  is also drawn with a dashed black line, as a reference. The shaded grey region marks the range where numerical effects strongly affect the shape of  $P_{E_{\perp}}$ .

nent,  $\mathbf{B}_{\parallel}$  (red dot-dashed), of the density fluctuations,  $n$  (purple) and of the total current density,  $\mathbf{J}$  (grey). The density and the parallel magnetic fluctuations are strongly coupled beyond  $k_{\perp}d_p \sim 2$ . In the MHD range, they exhibit a flat spectrum, which is approximately an order of magnitude smaller than the one of the perpendicular magnetic fluctuations. Therefore, the large-scale activity has little contribution from compressible fluctuations – although they can still play a significant role in the dynamics of the out-of-plane components – and the magnetic compressibility, i.e., the ratio of parallel to total magnetic fluctuations, is also negligible at small  $ks$ . Both spectra steepen at sub-proton scales, following a clean power-law scaling with a spectral index of  $-2.8$ . Note that their relative power level with respect to other fields' spectra increases, with  $P_{\mathbf{B}_{\parallel}}$  (and also  $P_{|\mathbf{B}|}$ ) becoming comparable with the spectrum of the perpendicular component,  $\mathbf{B}_{\perp}$  (cf. Fig. 4).

The spectral shape of the current density,  $\mathbf{J}$ , can be understood by recalling that  $\mathbf{J} = \nabla \times \mathbf{B}$ . A simple order-of-magnitude estimate of its perpendicular and parallel components gives  $\mathbf{J}_{\perp} \propto k_{\perp} \mathbf{B}_{\parallel}$  and  $\mathbf{J}_{\parallel} \propto k_{\perp} \mathbf{B}_{\perp}$ , respectively. Therefore, in the inertial range, where the magnetic activity is dominated by the perpendicular fluctuations, the spectrum of  $\mathbf{J}$  is determined by its parallel component  $\mathbf{J}_{\parallel}$  and this results in the observed spectral index of  $+1/3$ , since  $P_{\mathbf{J}_{\parallel}} \propto k_{\perp}^2 P_{\mathbf{B}_{\perp}}$ , with  $P_{\mathbf{B}_{\perp}} \propto k_{\perp}^{-5/3}$ . On the contrary, as already discussed,  $P_{\mathbf{B}_{\parallel}}$  and  $P_{\mathbf{B}_{\perp}}$  are comparable at sub-proton scales, both showing a power-law scaling, with spectral indices of  $-2.8$  and  $-3$ , respectively. The corresponding components,  $\mathbf{J}_{\parallel}$  and  $\mathbf{J}_{\perp}$ , are of the same order and exhibit a similar scaling, therefore  $P_{\mathbf{J}} \sim P_{\mathbf{J}_{\parallel}} \sim P_{\mathbf{J}_{\perp}}$ , and the corresponding scaling is in-between  $\propto k^{-0.8}$  and  $\propto k^{-1}$ . The change in the spectral slope of  $P_{\mathbf{J}}$  at  $k_{\perp}d_p \sim 2$  provides a further evidence of a spectral break in the magnetic field spectrum at proton scales.

Finally, the spectrum of the perpendicular electric fluctuations is reported in Fig. 7, as a green line. We choose

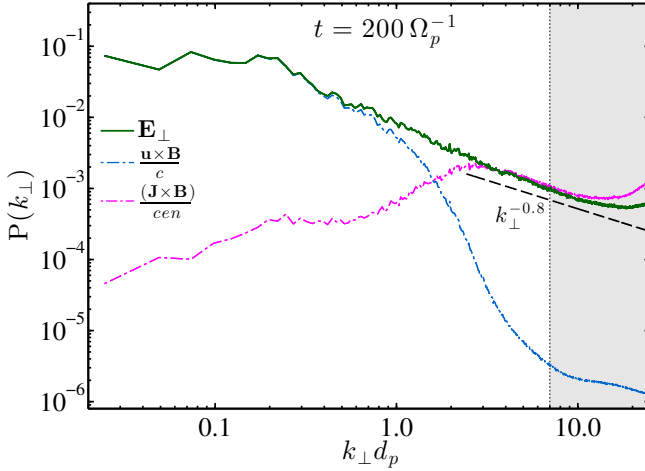


FIG. 8.— Spectrum of the perpendicular electric field,  $\mathbf{E}_{\perp}$ , as in Fig. 7, for the case with  $\beta_e = 0$  ( $\nabla p_e = 0$ ).

to pay particular attention to the electric field for three main reasons. Uppermost, it is expected to exhibit the most complex spectrum, since it contains the contributions of four terms having different relative importance in different ranges of scales. Secondly, it is the quantity that is mostly affected by both numerical effects and particle properties, so its behavior needs to be analyzed carefully, especially at small scales. Lastly, no consistent observational data about the properties of  $\mathbf{E}$  are available yet, so making predictions about the shape of its spectrum can be relevant for future analysis. We recall here that, starting from the Vlasov-fluid equations and assuming that the electrons act as a massless, charge-neutralizing fluid, the electric field can be computed from the generalized Ohm's law as

$$\mathbf{E} = -\underbrace{\frac{\mathbf{u} \times \mathbf{B}}{c}}_{\mathbf{E}_{\text{MHD}}} + \underbrace{\frac{\mathbf{J} \times \mathbf{B}}{cen}}_{\mathbf{E}_{\text{Hall}}} - \underbrace{\frac{\nabla p_e}{en}}_{\mathbf{E}_{\text{pe}}} + \underbrace{\eta \mathbf{J}}_{\mathbf{E}_\eta}. \quad (6)$$

In Fig. 7, together with  $P_{\mathbf{E}_{\perp}}$  obtained from numerical data, we also report the energy associated to the first three terms of Eq. (6), computed a-posteriori and drawn with cyan, magenta and black dot-dashed lines respectively (the contribution from the resistive term is negligible at all scales, since the resistive coefficient  $\eta$  is  $5 \times 10^{-4}$ .) At large scales,  $P_{\mathbf{E}_{\perp}}$  is clearly dominated by the MHD term,  $\mathbf{E}_{\text{MHD}}$ , which is essentially perpendicular to  $\mathbf{B}_0$ , since its leading contribution comes from  $\mathbf{u}_{\perp} \times \mathbf{B}_0$  ( $\mathbf{u}_{\perp} \times \mathbf{B}_{\parallel}$  and  $\mathbf{u}_{\parallel} \times \mathbf{B}_{\perp}$  are both of the second-order in the fluctuations). Therefore,  $P_{\mathbf{E}_{\perp}}$  follows strictly the spectrum of the perpendicular velocity fluctuations (cf. Fig. 4). Approximately at  $k_{\perp} d_p \sim 0.5$ , these two spectra decouple, since the second and third terms of Eq. (6) start contributing.

We can accurately analyze the Hall term,  $\mathbf{E}_{\text{Hall}}$ , by considering its perpendicular and parallel components separately. The former is of the first-order in the fluctuations, being led by  $(\mathbf{k}_{\perp} \times \mathbf{B}_{\parallel}) \times \mathbf{B}_0$  (other contributions are quadratic in  $\mathbf{B}_{\parallel}$  and  $\mathbf{B}_{\perp}$ , and therefore negligible). On the contrary, the latter is only of the second-order in the fluctuations, having the only contribution from  $(\mathbf{k}_{\perp} \times \mathbf{B}_{\parallel}) \times \mathbf{B}_{\perp}$ . Therefore, we expect the Hall term to

be negligible at large scales, where  $\mathbf{J}_{\perp}$  is small, and to exhibit a power-law behavior at small scales, with spectral index  $\sim -0.8$  following from  $E_{\text{Hall}} \propto k_{\perp}^2 P_{\mathbf{B}_{\parallel}}$ . Indeed, this is what we observe in Fig. 7 (compare the magenta dot-dashed line with the reference dashed black line). The electron pressure gradient term,  $\mathbf{E}_{\text{pe}}$ , has only perpendicular components by construction (our 2D computational domain is perpendicular to  $\mathbf{B}_0$ ). In the inertial range, it is of course negligible, the spectrum of the density fluctuations being essentially flat (compare with Fig. 4). On the contrary, at small scales, it is expected to give a contribution  $P_{\nabla n} \propto k_{\perp}^2 P_n$ , which has exactly the same slope as the contribution from the Hall term, since the spectra of the density fluctuations and of the parallel magnetic fluctuations have the same spectral index of  $-2.8$  at sub-proton scales. This is indeed what we observe in Fig. 7, where the contribution from the electron pressure gradient term is drawn with a black dot-dashed line. We would expect a similar behavior for  $P_{\mathbf{E}_{\perp}}$  at sub-proton scales, i.e., a power law with a spectral index of  $\sim -0.8$ , and we observe a hint of a similar scaling in the range  $2 \lesssim k_{\perp} d_p \lesssim 7$ .

The spectrum of the electric field fluctuations is the most affected by numerical effects among all the considered spectra, since the computation of  $\mathbf{E}$  involves both other fields ( $\mathbf{u}$  and  $\mathbf{B}$ ) and derivatives ( $\nabla \times \mathbf{B}$  and  $\nabla n$ ), as shown by Eq. (6). We already noticed that  $P_{\mathbf{B}}$  suffers from an accumulation of energy at small scales, which is only a numerical artifact, and so does  $P_{\mathbf{J}}$  (cf. Fig. 6). Moreover, derivatives in the numerical code are computed as finite differences, thus they are not able to recover very precise quantities at very small scales. For all these reasons, we cannot extract any robust information about the spectrum of the electric field at high wavevectors. In order to emphasize this, we choose to mark the “non-safety area”, which we estimate as  $k_{\perp} d_p \gtrsim 7$ , with a shaded gray region in Fig. 7.

Under particular conditions, i.e.,  $T_e = 0$ , one can obtain a better defined scaling for the electric field. In this case, the electron pressure gradient term,  $\mathbf{E}_{\text{pe}}$ , in the Ohm's law is zero (see Eq. (6)). Consequently, the level of the electric field spectrum at small scales is higher, since it is supported only by the Hall term  $\mathbf{E}_{\text{Hall}}$ . This can be seen in Fig. 8, where we show the same analysis of the electric field spectrum as in Fig. 7, but for a case with  $\beta_e = 0$  and all the other parameters set as in Run A. The electric field spectrum is now the sum of only two main contributions,  $\mathbf{E}_{\text{MHD}}$  and  $\mathbf{E}_{\text{Hall}}$ . No qualitative changes are introduced with respect to the case with a finite electron temperature; the former term dominates the spectrum at MHD scales, while the latter is responsible for the flattening of the electric field at ion scales. The important difference with respect to Run A, is that  $P_{\mathbf{E}_{\perp}}$  displays now a well defined power-law slope with an index of  $-0.8$ , consistent with the expectation. We expect the same slope also for the finite  $T_e$  case of Run A, in the absence of the numerical limitations discussed above.

#### 4. ROLE OF NUMERICAL PARAMETERS

##### 4.1. Spectral properties

As mentioned, a small numerical resistivity,  $\eta$ , has been implemented in all runs (see Table 1). A proper level of

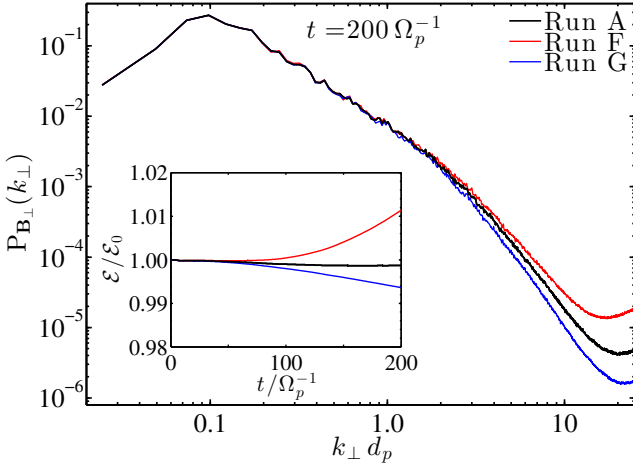


FIG. 9.— Power spectra of the perpendicular magnetic fluctuations,  $\mathbf{B}_\perp$ , for simulations with different values of the resistivity, i.e., Run A, ( $\eta = 5 \times 10^{-4}$ , black line), Run F ( $\eta = 1 \times 10^{-4}$ , red line) and Run G ( $\eta = 1 \times 10^{-3}$ , blue line).

resistivity is mandatory in order to prevent an accumulation of the energy in magnetic fluctuations at small scales, due to numerical errors. Runs F and G have been used to fine-tune the resistivity coefficient, starting from an order-of-magnitude estimate, and are characterized by the values  $\eta = 1 \times 10^{-4}$  and  $1 \times 10^{-3}$ , respectively. In Fig. 9, we show the corresponding spectra of the perpendicular magnetic fluctuations,  $\mathbf{B}_\perp$ , at  $t = 200 \Omega_p^{-1}$ , in comparison with Run A ( $\eta = 5 \times 10^{-4}$ ). For the setting adopted, the dissipative scale for the under-resistive case (Run F) can be estimated as  $k_{\text{dis}} d_p \sim 35$ , i.e., smaller than the scale corresponding to the employed resolution. As a consequence, this value of the resistivity is not high enough to remove the energy excess at small-scales, as also demonstrated by the shape of the spectrum of Run F in the sub-proton range. The over-resistive simulation (Run G) corresponds to the opposite case, where  $k_{\text{dis}} d_p \sim 6$ , thus well inside the range of wavevectors resolved in the simulation, making  $P_{\mathbf{B}_\perp}$  decreasing exponentially below the ion-break, a clear indication of a too strong dissipative damping at sub-proton scales. Lastly, the intermediate case, i.e., Run A, is expected to introduce a dissipation scale  $k_{\text{dis}} d_p \sim 10$ , allowing for the best description of the spectrum of  $\mathbf{B}_\perp$ . Indeed, this is observed to follow a power-law scaling with a spectral index of  $-3$  for roughly a decade after the break (cf. Fig. 4), in good agreement with solar wind spectra from observational data. Therefore, we decided to adopt  $5 \times 10^{-4}$  as the optimal value for the resistive coefficient  $\eta$ .

As a further confirmation for the adequacy of our choice for  $\eta$ , in the insert of Fig. 9 we also show the time evolution of the total energy  $\mathcal{E}$ , normalized to its initial value, for the same three simulations. In all three cases, the total energy stays constant for  $t \lesssim 70 \Omega_p^{-1}$ , while a different behavior is observed at later times. When the resistivity is too low (Run F, red line)  $\mathcal{E}$  grows significantly, due to the inefficient control of energy at small scales, and such an increase is already of the order of  $\sim 1\%$  at  $t = 200 \Omega_p^{-1}$ . On the contrary, when  $\eta$  is too high (Run G, blue line) the action of resistivity is too strong. Note that part of the energy subtracted from the

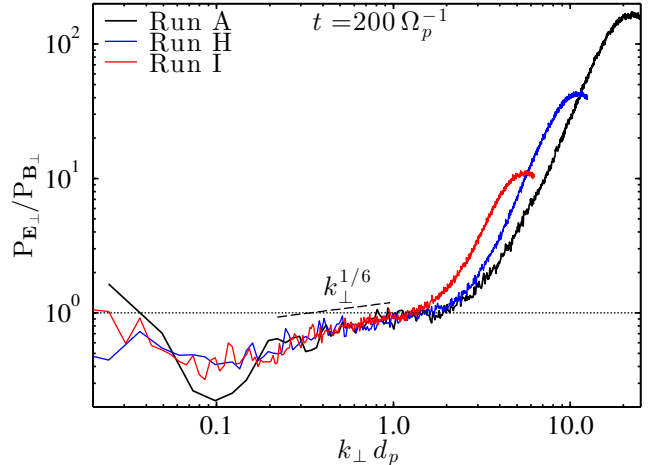


FIG. 10.— Ratio between the omnidirectional spectra of perpendicular electric fluctuations,  $P_{\mathbf{E}_\perp}$ , and perpendicular magnetic fluctuations,  $P_{\mathbf{B}_\perp}$ , for simulations with different resolution: Run A, with  $\Delta x = 0.125 d_p$  (black line), Run H, with  $\Delta x = 0.25 d_p$  (blue line), and Run I, with  $\Delta x = 0.5 d_p$  (red line).

magnetic fluctuations would also go into electron heating but, since the hybrid approximation does not provide an evolution for the electron temperature, such energy is not taken into account, and is then lost by the system, resulting in a net decrease of  $\mathcal{E}$ . The value  $\eta = 5 \times 10^{-4}$  is the one which better ensures the conservation of the total energy, with a relative difference between the beginning and the end of the simulation, i.e.,  $t = 500 \Omega_p^{-1}$ , of about 0.3%. Also note that, although the shape of  $P_{\mathbf{B}_\perp}$  at sub-proton scales is quite strongly affected by the resistivity, the power-law scaling in the inertial range and the position of the spectral break are not, assuring the reliability of the spectra shown in Fig. 4 and Fig. 5.

We also investigated the stability of omnidirectional spectra versus the spatial resolution. This was done by varying  $\Delta x$ , while keeping fixed the number of grid points (the total box length is then larger for larger grid spacing), as well as the amplitude of the initial magnetic fluctuations,  $B^{\text{rms}}$ . Run H and I implement  $\Delta x = 0.250$  and  $0.500 d_p$ , respectively (see Table 1). For both these runs, the value of the resistivity coefficient was suitably rescaled in order to get dissipation at the proper scales (note that  $\eta \propto \Delta x$  under these conditions).

In Fig. 10, the ratio between the omnidirectional spectra of the perpendicular electric and magnetic fluctuations,  $P_{\mathbf{E}_\perp}/P_{\mathbf{B}_\perp}$ , is compared between Run A, H and I. For all the three runs, this ratio exhibits the same scaling in the inertial range, following a power law with a spectral index of  $1/6$ . This is a direct consequence of the different scaling for the magnetic field ( $-5/3$ ) and the velocity ( $-3/2$ ) in the ideal MHD regime – where also  $P_{\mathbf{E}_\perp} \sim P_{\mathbf{u}_\perp}$  – leading then to a spectral index of  $-3/2 + 5/3 = 1/6$  for their ratio. As the other terms in the generalized Ohm’s law became important at ion scales, the  $P_{\mathbf{E}_\perp}/P_{\mathbf{B}_\perp}$  ratio increases significantly at smaller  $ks$ . Interestingly, increasing  $\Delta x$  from  $0.125$  (blue) to  $0.250 d_p$  (black) does not produce a change in the scale at which  $P_{\mathbf{E}_\perp}$  exceeds  $P_{\mathbf{B}_\perp}$ , and this break is observed to occur at  $k_\perp d_p \sim 2$  in both cases. Moreover, the two curves exhibit similar slopes in the sub-proton ranges. This is a confirmation that the estimate of  $\eta$

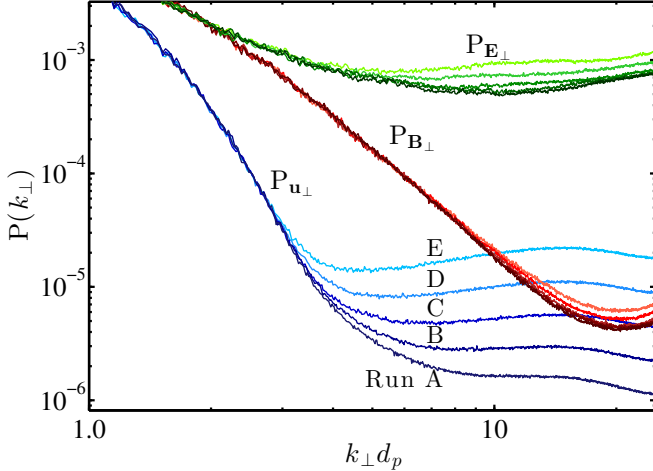


FIG. 11.— Zoom of the power spectra of the perpendicular magnetic, electric and proton bulk velocity fluctuations (drawn with red, green and blue lines, respectively) at small scales, where the contribution of numerical noise is not negligible. Lines with different shades of the same color correspond to simulations with different amounts of ppc, ranging from 500 to 8000, with darker colors being associated with a higher number of particles.

for the two simulations was correct and that the raise in  $P_{E\perp}/P_{B\perp}$  is physical and well captured by the runs. On the other hand, when employing a lower resolution,  $\Delta x = 0.500$  (red), the break seems to occur at slightly larger scales. This is likely a consequence of the reduction of the resolution at small scales: in Run I, the break and the dissipative scale are not well separated in Fourier space, so that subtracting energy at the smallest scales via resistive dissipation also affects the shape of the spectra around  $k_\perp d_p \sim 2$ , where the break occurs. This is an evidence that the scaling for the spectra discussed and shown in Fig. 4, continue to hold at lower spatial resolution, but also that  $\Delta x \gtrsim 0.500 d_p$  is not sufficient to properly explore the physical behavior at sub-ion scales.

Finally, the importance of employing a high number of particles was investigated, by keeping all the same parameters as for Run A except for varying the number of ppc from 4000 to 500 in steps of a factor of 2 (Runs from B to E in Table 1). In Fig. 11, the spectra of the perpendicular velocity, magnetic and electric fluctuations are reported with lines in different shades of blue, red and green respectively, corresponding to simulations with different numbers of ppc ranging from 500 (lighter color, Run E) to 8000 (darker color, Run A). Increasing the number of pcc from 500 ( $\sim 2.0 \times 10^9$  total particles) to 8000 ( $\sim 3.3 \times 10^{10}$  total particles) results in an decrease of the noise at small scales of more than one order of magnitude for the spectrum of the perpendicular velocity fluctuations. On the other hand, the trend of the spectrum up to the proton inertial length and slightly above is not affected, and the curve corresponding to our most accurate simulation (Run A) overlaps with the one with 4000 ppc (Run B) up to  $k_\perp d_p \sim 4$ . On the contrary, the spectrum of the perpendicular magnetic fluctuations is only barely affected by the numerical noise when the number of particles is sufficiently high, since the curves for 4000 and 8000 ppc are almost indistinguishable, proving that the number of ppc employed in Run A is sufficient to get reliable results for  $P_{B\perp}$  up to  $k_\perp d_p \sim 10$ .

Lastly, the spectrum of the perpendicular electric fluctuations shows a dependence on the number of particles at scales  $k_\perp d_p \gtrsim 4$ , but the curves for 4000 and 8000 ppc are quite close to each other even at smaller scales. However, as mentioned,  $P_{E\perp}$  is influenced by different sources of numerical noise, and all contribute in affecting the spectrum at small scales. We would like to stress that the evaluation of the noise due to the finite number of ppc only represents a lower limit of the overall noise, and therefore our previous choice of marking a shaded grey area for  $k_\perp d_p \gtrsim 7$  in Fig. 7 is not in contrast with these results.

#### 4.2. Proton heating

Fig. 1 shows that some particle heating is observed during the turbulent activity. Some care must be used in the interpretations of this result, since it may be significantly affected by some of the numerical settings. Therefore, we carefully consider the properties of the proton heating in this subsection.

Resistivity is observed to play a fundamental role in determining the overall proton heating,  $\Delta T_{\parallel,\perp} = \langle T_{\parallel,\perp} \rangle - T_0$ , and the proton temperature anisotropy,  $A_p$ . In Fig. 12, we show the time evolution of the perpendicular  $T_{p\perp}$  and the parallel  $T_{p\parallel}$  proton temperature, in solid and dashed lines, respectively, corresponding to different values of the resistive coefficient  $\eta$  (Run A, F and G of Table 1). The time evolution of  $T_{p\parallel}$  is observed to be not affected almost at all by the resistivity, showing an early decrease up to  $t \sim 50 \Omega_p^{-1}$  and then an increase with an almost constant rate, as was already shown for Run A in Fig. 1. The situation is different for  $T_{p\perp}$ , since its behavior for different values of  $\eta$  is the same only during the initial readjustment of the system, while it starts to differ after  $t \sim 40 \Omega_p^{-1}$ . At later times,  $T_{p\perp}$  exhibits a growth rate very similar to that of  $T_{p\parallel}$  for Run A (black), so no preferential perpendicular or parallel heating is observed. In particular,  $\Delta T_{p\perp}/T_0$  at  $t = 200 \Omega_p^{-1}$  is about 3.5%, while the corresponding  $\Delta T_{p\parallel}/T_0$  is about 2%. When  $\eta$  is lower (Run F, red),  $T_{p\perp}$  grows with a much faster rate than  $T_{p\parallel}$  for  $t \gtrsim 50 \Omega_p^{-1}$ , generating a strong preferential heating in the perpendicular direction,  $T_{p\perp}$  being about 8% greater than the initial value at  $t = 200 \Omega_p^{-1}$ . On the contrary, when  $\eta$  is higher (Run G, black lines),  $T_{p\perp}$  grows much slower, being overcome by  $T_{p\parallel}$  just before  $t = 200 \Omega_p^{-1}$ , leading to  $A_p < 1$  at later times. The amount of perpendicular heating observed is then significantly related to the presence of an excess of fluctuations at small scales, and can be then therefore largely overestimated, or underestimated, if an incorrect value of the resistivity is adopted.

The perpendicular proton heating is also found to be strongly affected by the number of particles employed. In Fig. 13, we report the ratio  $\Delta T_{p\perp}/T_0$ , where  $\Delta T_{p\perp} = \langle T_{p\perp} \rangle - T_0$  is computed at  $t = 200 \Omega_p^{-1}$ , versus the number of ppc for Runs from A to E (see Table 1). At this time,  $\Delta T_{p\perp}/T_0$  is clearly higher when employing a lower number of ppc. In particular, while a good convergence towards a value of  $\sim 3.4\%$  is observed when increasing the number of ppc from 4000 to 8000, this quantity clearly diverges when few particles are employed, reaching 4.8% for 500 ppc. Moreover, the difference in  $T_{p\perp}$

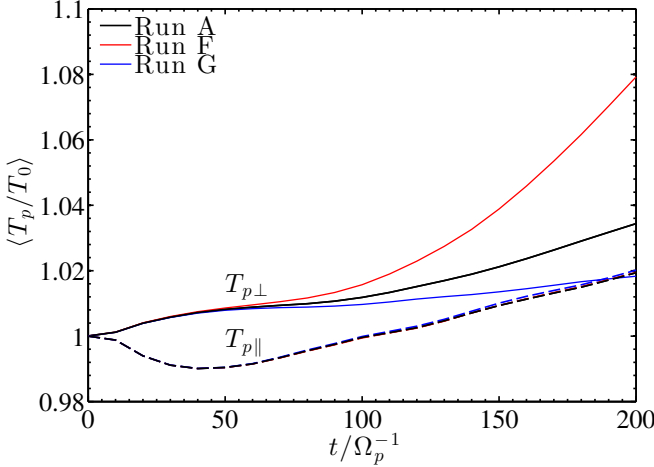


FIG. 12.— Time evolution of the parallel and perpendicular proton temperature,  $T_{p\parallel}$  and  $T_{p\perp}$ , respectively, normalized to the initial common value,  $T_0$ . The evolution is here shown for different values of the resistive coefficient (see Table 1). Solid and dashed lines are used for  $T_{p\perp}$  and  $T_{p\parallel}$ , respectively.

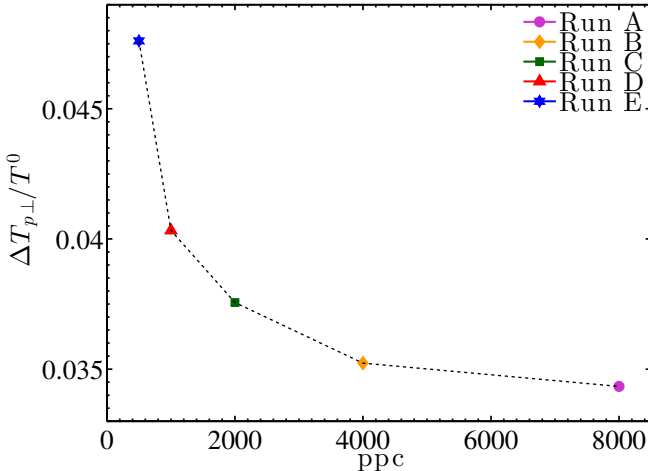


FIG. 13.— Perpendicular proton heating,  $\Delta T_{p\perp} / T_0$ , computed at  $t = 200 \Omega_p^{-1}$ , versus the number of ppc employed, ranging from 8000 (Run A) to 500 (Run E).

between Run A and Run E tends to further increase at later times. The main result of this analysis is that the use of a high number of ppc is mandatory when trying to give an estimate of  $T_{p\perp}$ , which could be largely overestimated otherwise. On the contrary, the parallel proton temperature is found to be largely independent from the number of particles (the relative difference between Run A and Run E is lower than 0.1% at  $t = 200 \Omega_p^{-1}$ ).

To conclude our analysis, we find that the spatial resolution  $\Delta x$  does not seem to affect significantly the proton heating, provided that the value of the resistivity is suitably set as discussed in Subsection 4.1. Differences between  $T_{p\perp}$  at  $t = 200 \Omega_p^{-1}$  for Runs A, H, and I are less than 0.6%. The dependency of  $T_{p\parallel}$  on the spatial resolution is also negligible.

## 5. SUMMARY AND CONCLUSIONS

In this work, we have presented properties of turbulence in a magnetized collisionless plasma by means of

two-dimensional hybrid PIC simulations, extending the results of Letter 1. Remarkably, our simulations implement a high number of collocation points ( $2048 \times 2048$ ) and a very high number of particles (up to 8000 ppc), covering a large simulation domain (not less than  $L_{\text{box}} = 256 d_p$ ) with a fine spatial resolution. This enables to self-consistently describe the evolution of turbulence over three orders of magnitude in wavevectors, and to fully capture its transition from fluid-like MHD scales to kinetic sub-ion scales, by using a single simulation (see Letter 1).

The adopted initial conditions consist of balanced and equipartitioned magnetic and velocity fluctuations, i.e., with zero cross helicity and zero residual energy. The onset of a turbulent cascade appears quite early during the simulations ( $t \sim 200 \Omega_p^{-1}$ , corresponding to approximatively 10 nonlinear times  $t_{\text{NL}}$ ), i. e., when most of the initial modes have started to partake into the cascade. In physical space, the activity of turbulence is characterized by magnetic field coherent structures, vortices, and strong and localized current sheets at smaller scales.

Generation of coherent structures associated to intermittency is observed as turbulence evolves through MHD to sub-proton scales. PDFs of increments of a perpendicular component of the magnetic fluctuations at  $t = 200 \Omega_p^{-1}$  exhibit a deviation from the normal distribution at all scales. This is small in the inertial range, becoming larger in correspondence of the spectral break at  $k_{\perp} d_p \sim 2$ , while at  $k_{\perp} d_p \sim 2$  the PDF has a much leaner shape with long non-zero tails. The corresponding excess kurtosis confirms this behavior. It is very small around the injection scale, since part of the MHD range fluctuations still acts as an energy reservoir for turbulence at  $t = 200 \Omega_p^{-1}$ , while it increases through the inertial range. Moreover, we observe a further increase at smaller scales. Observational data give no firm results about the behavior of this quantity at different scales (Alexandrova et al. 2008a; Kiyani et al. 2009, 2013; Wu et al. 2013; Chen et al. 2014). Nevertheless, when shown, all previous simulations observe an increase of the kurtosis at smaller scales (e.g., Dmitruk & Matthaeus 2006; Wan et al. 2012; Karimabadi et al. 2013; Wu et al. 2013).

When looking at the spectra of the relevant quantities, two clear distinct turbulent regimes are observed. At larger scales, the magnetic field follows a Kolmogorov  $-5/3$  power law, while the velocity has a spectral index of  $-3/2$ , which is characteristic of a Iroshnikov-Kraichnan turbulence. An excess of magnetic energy with respect to the kinetic energy is observed throughout the inertial range. The two different scalings for the magnetic and velocity fluctuations, often observed in the solar wind (Podesta et al. 2006, 2007; Tassein et al. 2009; Salem et al. 2009; Chen et al. 2011b), are very stable in time. They appear at the maximum of the turbulent activity and persist throughout all the simulations, as the energy reservoir at large scales is able to sustain and maintain the cascade. In Letter 1, we showed that such magnetic and velocity scaling are also combined with a spectral index of  $-2$  for the residual energy, in agreement with observations in the solar wind (Chen et al. 2013a). Incompressible MHD (Müller & Grappin 2005) and Reduced MHD (Boldyrev et al. 2011) only partially reproduce such scaling. In our simulations, the 2D geometry

and the presence of compressibility may play a role in setting the different scaling.

A clear transition in the spectra is observed at scales  $k_{\perp} d_p \gtrsim 1$ , with a change in the spectral indices of all fields. In particular, the spectrum of the perpendicular magnetic fluctuations steepens at  $k_{\perp} d_p \sim 2$ , following a power law with spectral index  $\sim -3$  for another decade. The location of the break does not show any significant dependence on the number of particles, the spatial resolution and the resistivity adopted, provided that a sufficient number of grid points allows to cover approximately a decade at sub-proton scales, i.e., that the scale at which resistive dissipation acts is sufficiently separated from the region of the break. The parallel component of the magnetic field, together with the density, follows a similar but slightly shallower slope with a spectral index of  $\sim -2.8$ , in very good agreement with observations (Chen et al. 2012, 2013b) and other simulations (Howes et al. 2011; Passot et al. 2014). As a result, magnetic fluctuations tend to become isotropic at small scales, resulting in an increase of the magnetic compressibility, as observed in the solar wind (Salem et al. 2012; Podesta & TenBarge 2012; Kiyani et al. 2013). The spectrum of the perpendicular velocity fluctuations quickly drops above  $k_{\perp} d_p \sim 1$ , without any clear power-law trend. The observation of a spectral index of  $-2.8$  has been ascribed to the effect of the electron Landau damping by previous studies (Howes et al. 2011; Passot et al. 2014), however, this can not be the case in our simulations, where the electron kinetics is not taken into account. Alternatively, the presence of coherent structures, such as current sheets, can produce a steepening of the energy spectra (e.g., Wan et al. 2012; Karimabadi et al. 2013). The increase of intermittency at small scales, observed in our simulations, seems to confirm this path towards the dissipation. We have to note, however, that a  $-8/3$  power law for the magnetic energy and the density spectra (not far from the  $2.8$  found here) has been also interpreted as related to the dimensionality (1D or 2D) of the magnetic and the density intermittent structures, without invoking dissipation (Boldyrev & Perez 2012; Meyrand & Galtier 2013).

The spectrum of the electric fluctuations is highly dominated by its perpendicular component. It is strongly coupled to the spectrum of the perpendicular velocity fluctuations at fluid scales, then it decouples and flattens, exceeding the spectrum of the perpendicular magnetic fluctuations and becoming dominant for  $k_{\perp} d_p \gtrsim 2$ . At large scales, the only contribution comes from the MHD term in Eq. (6), whose leading term is

$$\mathbf{E}_{\perp} \propto \mathbf{u} \times \mathbf{B} \sim \mathbf{u}_{\perp} \times \mathbf{B}_0. \quad (7)$$

This corresponds to a power-law scaling

$$P_E \propto P_{u_{\perp}} \propto k_{\perp}^{-3/2}, \quad (8)$$

which is observed in the simulations, and is also consistent with observations (Chen et al. 2011a). In our case, the main contributions at sub-proton scales come from the Hall and the electron pressure gradient terms, since the spectrum of the velocity fluctuations is observed to drop exponentially at short wavelengths. The leading terms at these scales are, then,

$$\mathbf{J} \times \mathbf{B} - \nabla p_e \propto \nabla(T_e n + \mathbf{B}_0 \cdot \mathbf{B}_{\parallel}). \quad (9)$$

Note that, in general, the sum of the two terms inside parentheses would not necessarily result in a power law for the electric field. However, since in our simulations both  $n$  and  $\mathbf{B}_{\parallel}$  are observed to scale with the same power law – thanks to the strong coupling between the plasma and the magnetic compressibility – then the expected spectral index for the electric field is:

$$P_E \propto k_{\perp}^2 P_{B_{\parallel},n} \propto k_{\perp}^{-0.8}. \quad (10)$$

Although it is not possible to directly test this scaling for the electric field spectrum in Run A, individual terms in Eq. (5) follow well the prediction (see Fig. 7). Moreover, we were able to show that when assuming  $T_e = 0$  (i.e., setting to zero the electron pressure gradient term in the Ohm's law), then the electric field spectrum – hence dominated by the Hall term – follows a  $k_{\perp}^{-0.8}$  scaling in the sub-proton range (Fig. 8), being only very slightly affected by numerical effects at very small scales ( $k_{\perp} d_p \gtrsim 10$ ).

As a result of the interaction of particles with the turbulent fluctuations and small scale structures, we observe an overall parallel and perpendicular heating with similar rates, so that the temperature of the plasma remains globally nearly isotropic. This behavior can be achieved only if a high enough number of particles is employed, and the resistivity is properly set in order to assure an accurate conservation of the total energy and a clear power-law behavior for the spectrum of the magnetic fluctuations at all scales. The parallel temperature,  $T_{p\parallel}$ , is found to have a very robust evolution, being essentially independent of the resistivity, the number of particles, and the spatial resolution employed. On the contrary, the time evolution of  $T_{p\perp}$  is strongly determined by both the resistivity and the number of ppc: if too few particles are employed, or if the resistivity is too low, the perpendicular heating can be largely overestimated/unphysical. Conversely, when a too strong value of the resistivity is implemented, the artificial damping of fluctuations at ion scales can produce a strong reduction of the perpendicular heating, thus generating an equally unphysical preferential parallel heating. This proves that no firm conclusions can be drawn about the perpendicular heating by turbulence in hybrid simulations, unless a careful and empirically fine-tuned choice of all parameters has been taken.

Note, however, that the fact that we do not observe a global preferential heating does not imply the absence of signatures of localized preferential deformations of the particle distribution functions, as suggested by the bottom right panel of Fig. 2, where strong temperature anisotropies ranging from 0.5 to 1.8 are observed. They seem to be concentrated in regions with stronger coherent structures, identified by the presence of current sheets and a significant level of vorticity. These results are in agreement with previous works based on the Vlasov-hybrid approximation (e.g., Servidio et al. 2012; Perrone et al. 2013; Valentini et al. 2014; Servidio et al. 2014). As the overall heating is rather weak, slow, and nearly isotropic, we can infer that the local formation of large proton temperature anisotropies is likely due to energy exchanges between the parallel and perpendicular directions, and/or to the spatial transport, rather than due to the heating.

Solar wind observations show a certain variability of the spectral properties. In particular, the position of the break at ion scales and the shape of the magnetic field spectrum around it seems to depend on the power of magnetic fluctuations (Bruno et al. 2014) and on the plasma beta (Alexandrova et al. 2008a; Chandran et al. 2009; Chen et al. 2014). Investigating such a dependence, by exploring the parameter space of the level of fluctuations and the plasma beta, will be the subject of a forthcoming paper.

Three-dimensional simulations would be fundamental to further improve the present study and overcome its limitations, allowing for a more realistic description of the turbulent cascade.

The authors wish to acknowledge valuable discussions

with Olga Alexandrova, Chris Chen, Giuseppe Consolini, Roland Grappin, Frank Löffler, and Marco Velli. This project has received funding from the European Union's Seventh Framework Programme for research, technological development and demonstration under grant agreement no 284515 (SHOCK). Website: <http://project-shock.eu/home/>. This research was conducted with high performance computing (HPC) resources provided by the Louisiana State University (allocations hpc\_hyrel14 and hpc\_hyrel15) and by CINECA (grant HP10CVCUF1). P.H. acknowledges GACR grant 15-10057S. L.M. was funded by STFC grant ST/K001051/1. A.V. acknowledges the Interuniversity Attraction Poles Programme initiated by the Belgian Science Policy Office (IAP P7/08 CHARM).

## REFERENCES

- Alexandrova, O., Carbone, V., Veltri, P., & Sorriso-Valvo, L. 2008a, *ApJ*, 674, 1153  
 Alexandrova, O., Chen, C. H. K., Sorriso-Valvo, L., Horbury, T. S., & Bale, S. D. 2013, *Space Sci. Rev.*, 178, 101  
 Alexandrova, O., Lacombe, C., & Mangeney, A. 2008b, *Ann. Geophys.*, 26, 3585  
 Alexandrova, O., Lacombe, C., Mangeney, A., Grappin, R., & Maksimovic, M. 2012, *ApJ*, 760, 121  
 Alexandrova, O., Saur, J., Lacombe, C., Mangeney, A., Mitchell, J., Schwartz, S. J., & Robert, P. 2009, *Phys. Rev. Lett.*, 103, 165003  
 Bale, S. D., Kellogg, P. J., Mozer, F. S., Horbury, T. S., & Reme, H. 2005, *Phys. Rev. Lett.*, 94, 215002  
 Beinroth, H. J., & Neubauer, F. M. 1981, *J. Geophys. Res.*, 86, 7755  
 Beresnyak, A. 2011, *Phys. Rev. Lett.*, 106, 075001  
 Beresnyak, A., & Lazarian, A. 2009, *ApJ*, 702, 460  
 Biskamp, D., Schwarz, E., Zeiler, A., Celani, A., & Drake, J. F. 1999, *Phys. Plasmas*, 6, 751  
 Boldyrev, S., & Perez, J. C. 2012, *ApJ Lett.*, 758, L44  
 Boldyrev, S., Perez, J. C., Borovsky, J. E., & Podesta, J. J. 2011, *ApJ Lett.*, 741, L19  
 Bruno, R., & Carbone, V. 2013, *Living Rev. Solar Phys.*, 10, 2  
 Bruno, R., Trenchi, L., & Telloni, D. 2014, *ApJ Lett.*, 793, L15, L15  
 Camporeale, E., & Burgess, D. 2011, *ApJ*, 730, 114  
 Chandran, B. D. G., Quataert, E., Howes, G. G., Xia, Q., & Pongkitiwanichkul, P. 2009, *Astrophys. J.*, 707, 1668  
 Chang, O., Gary, P. S., & Wang, J. 2011, *Geophys. Res. Lett.*, 38, L22102  
 Chen, C. H. K., Bale, S. D., Salem, C., & Mozer, F. S. 2011a, *ApJ Lett.*, 737, L41  
 Chen, C. H. K., Bale, S. D., Salem, C. S., & Maruca, B. A. 2013a, *ApJ*, 770, 125  
 Chen, C. H. K., Boldyrev, S., Xia, Q., & Perez, J. C. 2013b, *Phys. Rev. Lett.*, 110, 225002  
 Chen, C. H. K., Horbury, T. S., Schekochihin, A. A., Wicks, R. T., Alexandrova, O., & Mitchell, J. 2010, *Phys. Rev. Lett.*, 104, 255002  
 Chen, C. H. K., Leung, L., Boldyrev, S., Maruca, B. A., & Bale, S. D. 2014, *Geophysical Research Letters*, 41, 8081  
 Chen, C. H. K., Mallet, A., Yousef, T. A., Schekochihin, A. A., & Horbury, T. S. 2011b, *MNRAS*, 415, 3219  
 Chen, C. H. K., Salem, C. S., Bonnell, J. W., Mozer, F. S., & Bale, S. D. 2012, *Phys. Rev. Lett.*, 109, 035001  
 Chen, C. H. K., Sorriso-Valvo, L., Šafránková, J., & Němeček, Z. 2014, *ApJ Lett.*, 789, L8  
 Cho, J., & Lazarian, A. 2004, *ApJ Lett.*, 615, L41  
 —. 2009, *ApJ*, 701, 236  
 Cranmer, S. R., Matthaeus, W. H., Breech, B. A., & Kasper, J. C. 2009, *ApJ*, 702, 1604  
 Dmitruk, P., & Matthaeus, W. H. 2006, *Phys. Plasmas*, 13, 042307  
 Dong, Y., Verdini, A., & Grappin, R. 2014, *ApJ*, 793, 118  
 Franci, L., Verdini, A., Matteini, L., Landi, S., & Hellinger, P. 2015, *ApJ Lett.*, 804, L39  
 Goldstein, M. L., Roberts, D. A., & Fitch, C. A. 1994, *J. Geophys. Res.*, 99, 11519  
 Gómez, D., Martín, L. N., & Dmitruk, P. 2013, *Adv. Space Res.*, 51, 1916  
 Gómez, D. O., Mahajan, S. M., & Dmitruk, P. 2008, *Phys. Plasmas*, 15, 102303  
 Grappin, R., Mangeney, A., & Marsch, E. 1990, *J. Geophys. Res.*, 95, 8197  
 Grappin, R., & Müller, W.-C. 2010, *Phys. Rev. E*, 82, 026406  
 Grappin, R., Velli, M., & Mangeney, A. 1991, *Ann. Geophys.*, 9, 416  
 Hellinger, P., Matteini, L., Štverák, Š., Trávníček, P. M., & Marsch, E. 2011, *J. Geophys. Res.*, 116, A09105  
 Hellinger, P., Trávníček, P., Kasper, J. C., & Lazarus, A. J. 2006, *Geophys. Res. Lett.*, 33, L09101  
 Hellinger, P., Trávníček, P. M., Štverák, Š., Matteini, L., & Velli, M. 2013, *J. Geophys. Res.*, 118, 1351  
 Howes, G. G., Dorland, W., Cowley, S. C., Hammett, G. W., Quataert, E., Schekochihin, A. A., & Tatsuno, T. 2008, *Phys. Rev. Lett.*, 100, 065004  
 Howes, G. G., Tenbarge, J. M., Dorland, W., Quataert, E., Schekochihin, A. A., Numata, R., & Tatsuno, T. 2011, *Phys. Rev. Lett.*, 107, 035004  
 Karimabadi, H., et al. 2013, *Phys. Plasmas*, 20, 012303  
 Kiyani, K. H., Chapman, S. C., Khotyaintsev, Y. V., Dunlop, M. W., & Sahraoui, F. 2009, *Phys. Rev. Lett.*, 103, 075006  
 Kiyani, K. H., Chapman, S. C., Sahraoui, F., Hnat, B., Fauvarque, O., & Khotyaintsev, Y. V. 2013, *ApJ*, 763, 10  
 Leamon, R. J., Smith, C. W., Ness, N. F., Matthaeus, W. H., & Wong, H. K. 1998, *J. Geophys. Res.*, 103, 4775  
 Leamon, R. J., Smith, C. W., Ness, N. F., & Wong, H. K. 1999, *J. Geophys. Res.*, 104, 22331  
 Lee, E., Brachet, M. E., Pouquet, A., Mininni, P. D., & Rosenberg, D. 2010, *Phys. Rev. E*, 81, 016318  
 MacBride, B. T., Smith, C. W., & Forman, M. A. 2008, *ApJ*, 679, 1644  
 Markovskii, S. A., & Vasquez, B. J. 2011, *ApJ*, 739, 22  
 Markovskii, S. A., Vasquez, B. J., & Chandran, B. D. G. 2010, *ApJ*, 709, 1003  
 Maron, J., & Goldreich, P. 2001, *ApJ*, 554, 1175  
 Marsch, E., Ao, X.-Z., & Tu, C.-Y. 2004, *J. Geophys. Res.*, 109, 4102  
 Marsch, E., Schwenn, R., Rosenbauer, H., Muehlhaeuser, K.-H., Pilipp, W., & Neubauer, F. M. 1982, *J. Geophys. Res.*, 87, 52  
 Martin, L. N., De Vita, G., Sorriso-Valvo, L., Dmitruk, P., Nigro, G., Primavera, L., & Carbone, V. 2013, *Phys. Rev. E*, 88, 063107  
 Mason, J., Cattaneo, F., & Boldyrev, S. 2008, *Phys. Rev. E*, 77, 036403  
 Matteini, L., Landi, S., Hellinger, P., Pantellini, F., Maksimovic, M., Velli, M., Goldstein, B. E., & Marsch, E. 2007, *Geophys. Res. Lett.*, 34, 20105  
 Matthaeus, W. H., Dmitruk, P., Smith, D., Ghosh, S., & Oughton, S. 2003, *Geophys. Res. Lett.*, 30, 2104  
 Matthaeus, W. H., & Velli, M. 2011, *Space Sci. Rev.*, 160, 145  
 Matthews, A. P. 1994, *J. Comp. Phys.*, 112, 102  
 Meyrand, R., & Galtier, S. 2013, *Phys. Rev. Lett.*, 111, 264501  
 Mininni, P. D., & Pouquet, A. 2007, *Phys. Rev. E*, 99, 1  
 Mininni, P. D., & Pouquet, A. 2009, *Phys. Rev. E*, 80, 025401  
 Müller, W.-C., Biskamp, D., & Grappin, R. 2003, *Phys. Rev. E*, 67, 066302  
 Müller, W.-C., & Grappin, R. 2005, *Phys. Rev. Lett.*, 95, 114502  
 Ng, C. S., Bhattacharjee, A., Germaschewski, K., & Galtier, S. 2003, *Phys. Plasmas*, 10, 1954

- Parashar, T. N., Servidio, S., Breech, B., Shay, M. A., & Matthaeus, W. H. 2010, *Phys. Plasmas*, 17, 102304
- Parashar, T. N., Shay, M. A., Cassak, P. A., & Matthaeus, W. H. 2009, *Phys. Plasmas*, 16, 032310
- Parashar, T. N., Vasquez, B. J., & Markovskii, S. A. 2014, *Phys. Plasmas*, 21, 022301
- Passot, T., Henri, P., Laveder, D., & Sulem, P.-L. 2014, *Eur. Phys. J. D.*, 68, 207
- Perez, J. C., & Boldyrev, S. 2009, *Phys. Rev. Lett.*, 102, 025003
- Perez, J. C., Mason, J., Boldyrev, S., & Cattaneo, F. 2012, *Phys. Rev. X*, 2, 041005
- Perrone, D., Valentini, F., Servidio, S., Dalena, S., & Veltri, P. 2013, *ApJ*, 762, 99
- . 2014, *Eur. Phys. J. D.*, 68, 209
- Podesta, J. J., & Borovsky, J. E. 2010, *Phys. Plasmas*, 17, 112905
- Podesta, J. J., Roberts, D. A., & Goldstein, M. L. 2006, *J. Geophys. Res.*, 111, A10109
- . 2007, *ApJ*, 664, 543
- Podesta, J. J., & TenBarge, J. M. 2012, *J. Geophys. Res.*, 117, A10106
- Rodriguez Imazio, P., Martin, L. N., Dmitruk, P., & Mininni, P. D. 2013, *Phys. Plasmas*, 20, 052506
- Sahraoui, F., Goldstein, M. L., Belmont, G., Canu, P., & Rezeau, L. 2010, *Phys. Rev. Lett.*, 105, 131101
- Sahraoui, F., Goldstein, M. L., Robert, P., & Khotyaintsev, Y. V. 2009, *Phys. Rev. Lett.*, 102, 231102
- Salem, C., Mangeney, A., Bale, S. D., & Veltri, P. 2009, *ApJ*, 702, 537
- Salem, C. S., Howes, G. G., Sundkvist, D., Bale, S. D., Chaston, C. C., Chen, C. H. K., & Mozer, F. S. 2012, *ApJ Lett.*, 745, L9
- Servidio, S., Osman, K. T., Valentini, F., Perrone, D., Califano, F., Chapman, S., Matthaeus, W. H., & Veltri, P. 2014, *ApJ Lett.*, 781, L27
- Servidio, S., Valentini, F., Califano, F., & Veltri, P. 2012, *Phys. Rev. Lett.*, 108, 045001
- Servidio, S., Valentini, F., Perrone, D., Greco, A., Califano, F., Matthaeus, W. H., & Veltri, P. 2015, *J. Plasma Phys.*, 81, 325810107
- Shaikh, D. 2009, *MNRAS*, 395, 2292
- Shaikh, D., & Shukla, P. K. 2009, *Phys. Rev. Lett.*, 102, 045004
- Shaikh, D., & Zank, G. P. 2009, *MNRAS*, 400, 1881
- Smith, C. W., Hamilton, K., Vasquez, B. J., & Leamon, R. J. 2006, *ApJ Lett.*, 645, L85
- TenBarge, J. M., & Howes, G. G. 2013, *ApJ Lett.*, 771, L27
- TenBarge, J. M., Howes, G. G., & Dorland, W. 2013, *ApJ*, 774, 139
- Tessein, J. A., Smith, C. W., MacBride, B. T., Matthaeus, W. H., Forman, M. A., & Borovsky, J. E. 2009, *ApJ*, 692, 684
- Tu, C.-Y., & Marsch, E. 1995, *Space Sci. Rev.*, 73, 1
- Valentini, F., Servidio, S., Perrone, D., Califano, F., Matthaeus, W. H., & Veltri, P. 2014, *Phys. Plasmas*, 21, 082307
- Vasquez, B. J., & Markovskii, S. A. 2012, *ApJ*, 747, 19
- Verdini, A., & Grappin, R. 2012, *Physical Review Letters*, 109, 025004
- Verscharen, D., Marsch, E., Motschmann, U., & Müller, J. 2012, *Phys. Plasmas*, 19, 022305
- Wan, M., et al. 2012, *Phys. Rev. Lett.*, 109, 195001
- Wicks, R. T., Horbury, T. S., Chen, C. H. K., & Schekochihin, A. A. 2011, *Phys. Rev. Lett.*, 106, 045001
- Wu, P., et al. 2013, *ApJ Lett.*, 763, L30